Bi-stability Detection in the Flow Around a Sphere by Means of Experiments and Lattice Boltzmann Simulations

Christian Bauer[1,2(✉)], Max Müller[1,2], Klaus Ehrenfried[1], and Claus Wagner[1,2]

[1] Institute of Aerodynamics and Flow Technology, German Aerospace Center, Göttingen, Germany
christian.bauer@dlr.de

[2] Institute of Thermodynamics and Fluid Mechanics, Technische Universität Ilmenau, Ilmenau, Germany

Abstract. With the aim to detect bi-stability in the highly separated flow around a sphere mounted on a cross-stream rod, wind tunnel measurements and numerical simulations with a Lattice Boltzmann method (LBM) are performed and compared. In both, LBM simulation and experiment, a bi-stable flow behaviour is detected at a Reynolds number of $\mathrm{Re} = 10^5$ based on the sphere diameter, the inflow velocity and the kinematic viscosity, whereas such behaviour is absent at Reynolds numbers as high as $\mathrm{Re} = 3 \times 10^5$. The bi-stable behaviour detected in the time series of the aerodynamic side force acting on the sphere for $\mathrm{Re} = 10^5$ is reflected by a bi-modal probability density function. For $\mathrm{Re} = 3 \times 10^5$, on the contrary, the probability density function is nearly Gaussian. Further, in agreement with the experiment, two counter-rotating vortex tubes originating from the intersection of the leeward and cross-stream rodward side of the sphere are generated.

1 Introduction

Unsteady forces acting on ground vehicles are currently studied in experiments with transient inflow conditions, e.g. on cars in full scale [1], or on simplified car models in wind tunnels [2]. Additionally, those effects are investigated with detached-eddy simulation (DES) studies, e.g. by Krajnović [3]. Moreover, there are unsteady forces induced by wake instabilities that occur in separated flows. With regard to ground vehicles, these wake instabilities lead to bi-stable forces. In wind tunnel experiments, this bi-stability is investigated using simplified car models, for example by Grandemange et al. [4] and Pavia et al. [5]. Gentile et al. [6] show that the wake instabilities are sensitive to even small misalignments. In terms of numerical simulations, such instabilities are investigated using

A. Dillmann et al. (Eds.): STAB/DGLR Symposium 2020, NNFM 151, pp. 441–450, 2021.
https://doi.org/10.1007/978-3-030-79561-0_42

direct numerical simulations (DNS) at low Reynolds numbers, as done by Bury and Jardin [7], with the assumption that the results are valid at higher Reynolds numbers as well. Additionally, a DES study performed by Constantinescu and Squires [8] suggests that numerical methods which are not resolving all flow scales might also be able to predict the dynamics of a separated wake. In the present case a Lattice Boltzmann method (LBM) simulation of the flow around a sphere mounted on a cross-stream rod (CSR) is performed. The corresponding experimental setup (described in detail in Müller et al. [9]) consists of a sphere mounted on an internal six-component balance attached to a CSR. The wind tunnel measurement performed by Müller et al. [9] provides information on the dynamical behaviour of a separated flow over a sphere at a CSR, which leads to bi-stable side forces at certain Reynolds numbers. In the following, the results obtained from the latter measurement are compared to the predictions by the LBM simulation in order to determine, whether experiment and simulation agree in detecting wake-induced bi-stable forces at similar Reynolds numbers.

2 Experimental Setup

The experimental setup, see Fig. 1, was initially designed to induce transient sinusoidal side winds with a four-wing gust generator called *wing system*. This wing system was installed in the test section of the experimental setup. It was located upstream of the test model at a distance of ten times the chord length of one wing (300 mm). However, as this paper focuses on the inherent unsteady aerodynamics of the wake of a sphere, the flaps remained at the same position at 0° incidence and therefore do not impose any crosswinds. The model itself was a sphere with a diameter of 100 mm mounted on a 6-component balance attached to a CSR with a diameter of 25 mm. The clearance between the sphere and the floor of the test section was 295 mm. The forces acting on the sphere were measured with a sampling rate of 1 kHz and each measurement lasted 100 s. The Reynolds number,

$$Re = \frac{U_\infty d}{\nu}, \tag{1}$$

with U_∞ being the inlet velocity, d the sphere diameter and ν the kinematic viscosity, was set in the wind tunnel control and kept constant by a margin of 0.5% of its set value. Results obtained for the Reynolds numbers 10^5, 2×10^5 and 3×10^5 were recorded. Additionally, oil-film visualisations were conducted in order to highlight the flow structure.

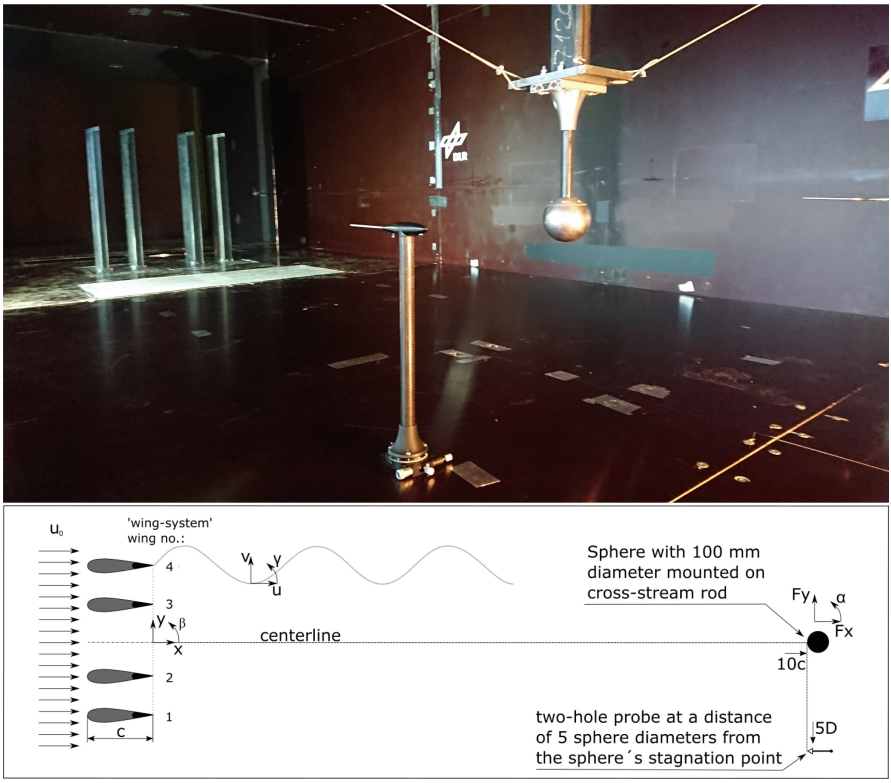

Fig. 1. Setup for the experimental investigation of the flow around a sphere mounted on a CSR with wing system. Top: picture of the test stand in the crosswind test facility (Seitenwindkanal Göttingen, SWG). Bottom: technical sketch of the test stand.

3 Numerical Methodology

As it has proven its ability to capture the dynamics of instationary, separated flows at Reynolds numbers as high as 3×10^5, the LBM was chosen to solve the governing equations via 3DS SIMULIA PowerFLOW®. In contrast to traditional methods of computational fluid mechanics, not the Navier-Stokes but the Lattice Boltzmann equations were solved in PowerFLOW®. The latter describe the dynamics of a particle velocity distribution function on a mesoscopic scale. Macroscopic quantities were then deducted via integration of mesoscopic variables. The discrete equations solved with the LBM read

$$f_i(\mathbf{x} + \mathbf{e}_i \Delta x, t + \Delta t) = f_i(\mathbf{x}, t) + \Omega_i(f(\mathbf{x}, t)), \quad i = 0, 1, \ldots, M, \tag{2}$$

where $\mathbf{x}$ is the location in space, t is the location in time, f_i is the particle velocity distribution function along the ith direction and Ω_i is the collision operator representing the rate of change of f_i due to collision [10]. Moreover, the collision

term is approximated by the Bhatnagar, Gross, and Krook model using a linear relaxation [11].

Similar to the Navier-Stokes equation, the LBM can be used for the DNS of fluid turbulence, when the lattice Δx resolves the smallest scales. Due to the high Reynolds numbers considered here, only large scales could be resolved, which corresponds to a large-eddy simulation in combination with subgrid-scale modelling and wall modelling. PowerFLOW® provides a two-equation model based on the turbulent kinetic energy k and dissipation ε. These two variables were used to derive turbulence quantities of the subgrid-scales, such as turbulent length scales $l = k^{3/2}/\varepsilon$, time scales $\tau = k/\varepsilon$ and turbulent viscosity $\nu_t = C_\mu k^2/\varepsilon$.

Complementing the experiments of Müller et al. [9], LBM simulations for the three Reynolds numbers were performed as presented in Table 1. The computational flow domain with dimensions $L_x \times L_y \times L_z = 45.4d \times 12.2d \times 8.3d$ consisted of seven different grid refinement levels with a refinement towards the sphere and the CSR. As boundary conditions a constant velocity U_∞ and turbulence intensity of $0.01U_\infty$ was given at the inlet, whereas a constant static pressure was set at the outlet. All other boundaries of the computational domain were modelled as "frictionless walls", i.e. impermeability and free-slip boundary conditions. The sphere and the CSR were both modelled as smooth solid walls. The flow domain was initialised with the modelled fluid air—having a kinematic viscosity $\nu = 1.568 \times 10^{-5}\,\mathrm{m}^2/\mathrm{s}$, a density $\rho = 1.17\,\mathrm{kg/m}^3$ and the speed of sound $c = 347.2\,\mathrm{m/s}$—at velocity U_∞ and turbulence intensity of $0.01U_\infty$.

Table 1. Simulation cases. $\mathrm{Re} = U_\infty d/\nu$ is the Reynolds number based on the sphere diameter d, the inlet velocity U_∞ and the kinematic viscosity ν. Δx_{min} is the minimum grid spacing. n is the number of time steps. Δt is the simulated physical time.

Case	Re	# voxels	$\Delta x_{min}/d$	n	$\Delta t U_\infty/d$
SR100	10^5	97.8×10^6	0.005	2.57×10^6	1944
SR200	2×10^5	97.8×10^6	0.005	2.58×10^6	1678
SR300	3×10^5	97.8×10^6	0.005	2.00×10^6	1940

4 Comparison of the Predicted and Measured Results

Time series of the force coefficients obtained from LBM simulations are depicted in Fig. 2. As indicated in Fig. 2a for $\mathrm{Re} = 10^5$, small scales in the drag force coefficient (C_x), as well as in the lift force coefficient (C_z), fluctuate around one constant average value, whereas the side force coefficient appears to be fluctuating with respect to two different values. The latter is also denoted as bi-stable behaviour. With increasing Reynolds number, this behaviour vanishes (Fig. 2b, c). For $\mathrm{Re} = 10^5$, instantaneous snapshots of the flow at each stable state are displayed in Fig. 3. Here, the wake flow behaviour at $t = 9.75\,\mathrm{s}$ (top) and at

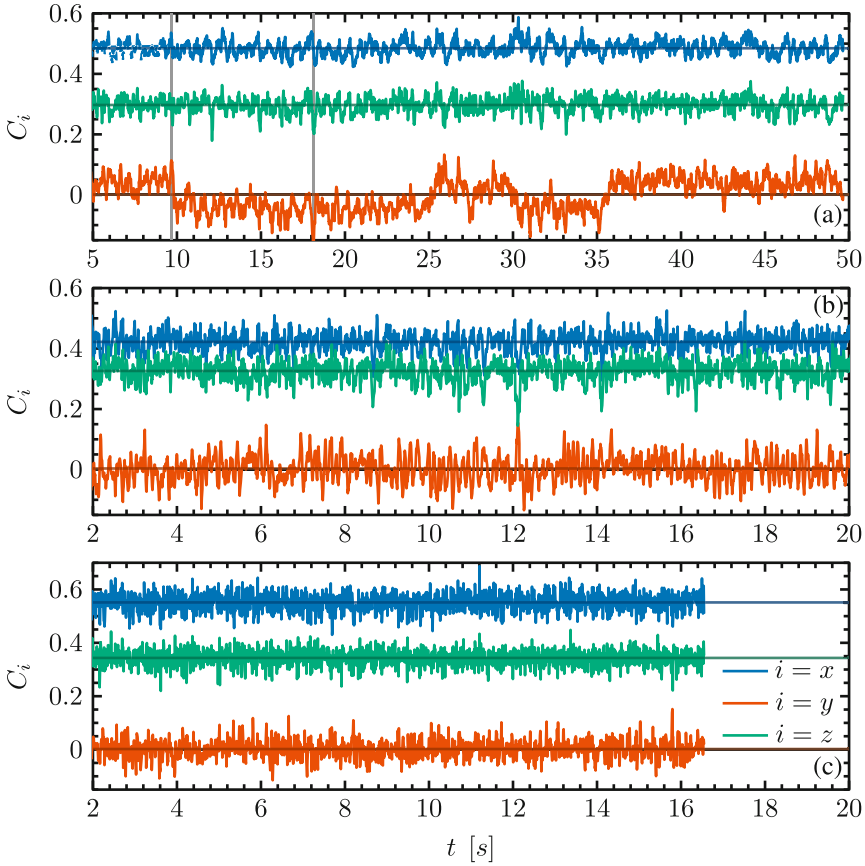

Fig. 2. Force coefficients predicted using LBM: —, C_x; —, C_y; —, C_z. (a) $\mathrm{Re} = 10^5$; (b) $\mathrm{Re} = 2 \times 10^5$; (c) $\mathrm{Re} = 3 \times 10^5$. Dark shaded lines indicate averaged values. Grey lines indicate times of snapshots in Fig. 3.

$t = 18.14\,\mathrm{s}$ (bottom) is visualised via iso-surfaces of the λ_2-criterion introduced by Jeong and Hussain [12]. As indicated by the grey auxiliary lines, the wake region is slightly skewed with respect to the y-axis, resulting in the side force reflected by the side force coefficient in Fig. 2a at corresponding times. The sign of the side force coefficient is determined by the direction in which the wake is skewed. Figure 4 presents the side and drag force coefficients obtained from the experiment. Note that the experimentally obtained side force coefficient time series have been filtered with a 10 Hz low-pass filter, a procedure further described in Müller et al. [9]. The observed bi-stability in the predicted side force coefficient at $\mathrm{Re} = 10^5$ matches the experimental data shown in Fig. 4a. Although the absolute values of the side force coefficient are higher in the experiment, the expected bi-stable behaviour can be observed in both data sets. Moreover, the time range in which the flow remains in one of the two stable states

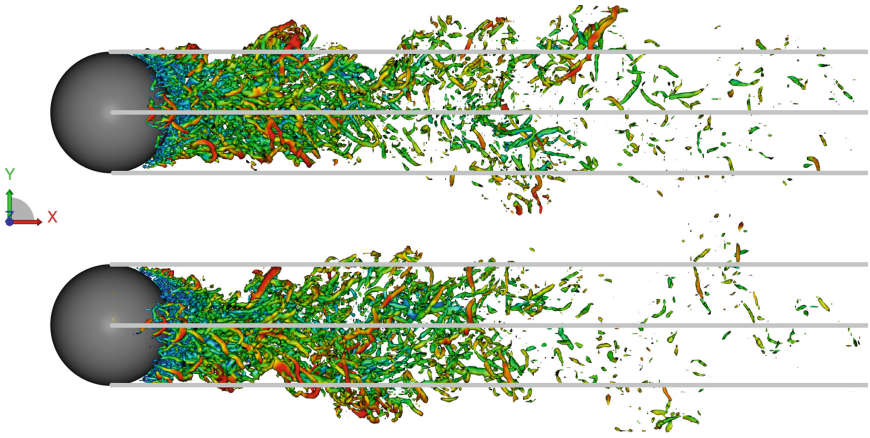

Fig. 3. Instantaneous flow field realisations showing iso-surfaces of the λ_2-criterion ($\lambda_2 = -10^5/\mathrm{s}^2$), coloured by the velocity magnitude ranging from 0 (blue) to U_∞ (red) for $\mathrm{Re} = 10^5$. View from top in negative z-direction. Top: Flow field at $t = 9.75\,\mathrm{s}$. Bottom: Flow field at $t = 18.14\,\mathrm{s}$. Grey lines indicate the sphere centreline and its horizontal boundaries.

is similar in the experimental and the numerical results for $\mathrm{Re} = 10^5$ (compare Figs. 2a and 4a). For $\mathrm{Re} = 2 \times 10^5$, the experimental side force coefficient shows a bi-stable behaviour with a strong tendency to one side (Fig. 4b), which is not predicted by the LBM simulations (Fig. 2b). For $\mathrm{Re} = 3 \times 10^5$, the side force coefficient shows no sign of bi-stability, neither in the experiment (Fig. 4c), nor in the LBM simulation (Fig. 2c). Further, the drag force coefficients obtained in the LBM simulation and the experiment are compared in Fig. 5, where they are plotted against the Reynolds number.

While the drag force coefficient deviates as much as 20% for $\mathrm{Re} = 2 \times 10^5$, the coefficients for the lowest and the highest Reynolds number agree better with deviations of ten percent and less than one percent for $\mathrm{Re} = 3 \times 10^5$ and $\mathrm{Re} = 10^5$, respectively. Due to the above-discussed deviations between the results obtained for $\mathrm{Re} = 2 \times 10^5$, only the lowest ($\mathrm{Re} = 10^5$) and the highest Reynolds number ($\mathrm{Re} = 3 \times 10^5$) are considered in the following analysis. Consequently, probability density functions (PDFs) are presented in Fig. 6 for the last mentioned Reynolds numbers.

The PDFs confirm the observations for the above-described time series statistically. Although the PDFs of the experiments and the LBM simulations do not collapse for $\mathrm{Re} = 10^5$ (Fig. 6a), both PDFs show a clear bi-stable behaviour. At $\mathrm{Re} = 3 \times 10^5$, the flow tends to become Gaussian, which is reflected in both PDFs, i.e. of the LBM simulation and the experiment. At this Reynolds number ($\mathrm{Re} = 3 \times 10^5$) no bi-stability is observed and the PDFs collapse nicely.

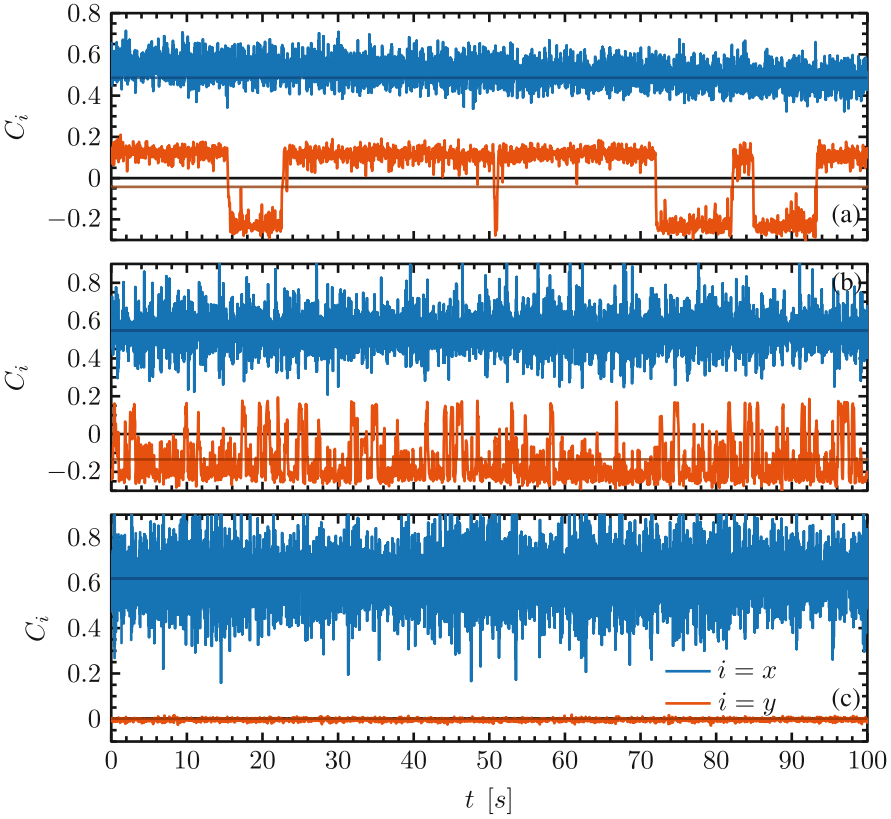

Fig. 4. Force coefficients from experiments: —, C_x; —, C_y. (a) Re = 10^5; (b) Re = 2×10^5; (c) Re = 3×10^5. Dark shaded lines indicate averaged values.

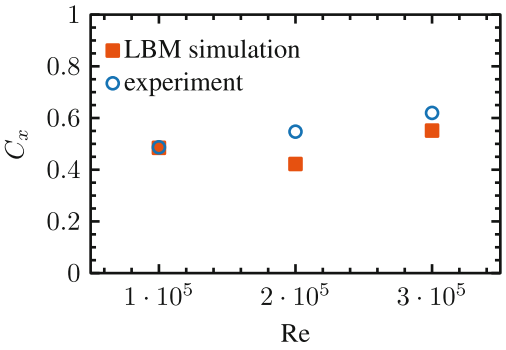

Fig. 5. Drag force coefficient C_x versus Reynolds number Re predicted in LBM simulations and measured in wind tunnel experiments.

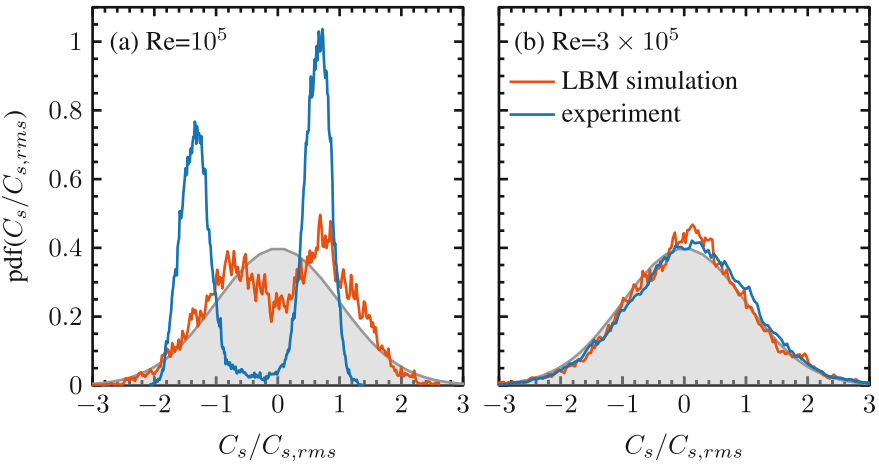

Fig. 6. Probability density functions of the side force coefficient. LBM simulation (—) and experiment (—) for $\mathrm{Re} = 10^5$ (a) and $\mathrm{Re} = 3 \times 10^5$ (b). Grey shaded areas indicate a Gaussian distribution $f(C_s/C_{s,rms}) = 1/(2\pi)^2 \cdot \exp\left[-0.5(C_s/C_{s,rms})^2\right]$.

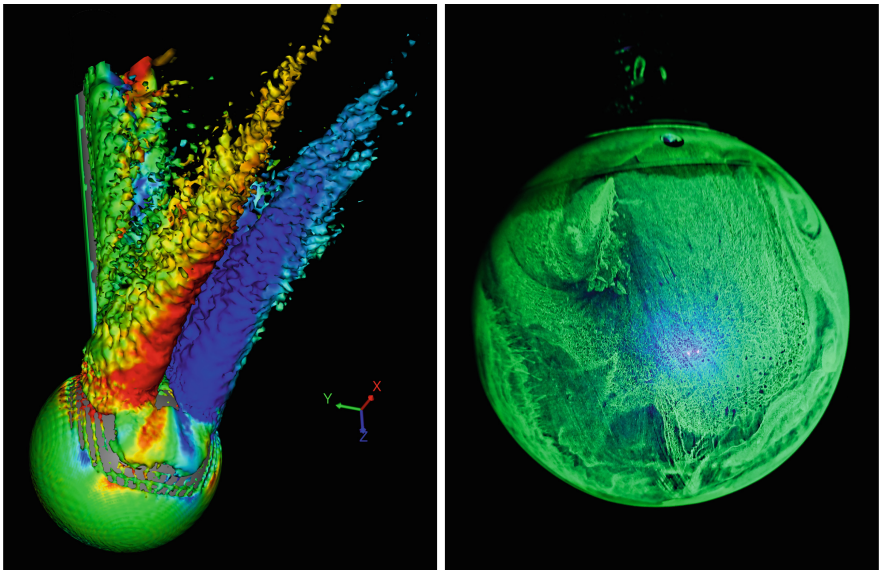

Fig. 7. Left: λ_2-iso-surface of the mean flow structure ($\lambda_2 = -7000/\mathrm{s}^2$) obtained from averaging over 500 snapshots at $\mathrm{Re} = 3 \times 10^5$. Pseudo-colours indicate the x-vorticity component ranging from $-300/\,\mathrm{s}$ (blue) to $300/\,\mathrm{s}$ (red). Right: Oil-film visualisation of the leeward side of a sphere at CSR at $\mathrm{Re} = 3 \times 10^5$ (yz-plane).

Finally, the average flow structure of the flow around a sphere mounted on a CSR at $\mathrm{Re} = 3 \times 10^5$ is considered. In the following, the average flow structure is visualised by means of the λ_2-criterion applied to an average flow field in the LBM simulation and by means of an oil film in the experiment (Fig. 7). Both visualisations (Fig. 7a and Fig. 7b) reflect a dual-vortex structure. The λ_2-isosurfaces in Fig. 7a depict two vortex tubes originating from the intersection of the leeward and the CSR-ward side of the sphere. The colouring of the vortex tubes by the x-vorticity indicates their rotational direction. Looking along the positive x-direction, the red-coloured vortex tube rotates counter-clockwise, whereas the blue-coloured one rotates clockwise. In addition, the footprint of these vortical structures can be seen in the oil-film visualisation shown in Fig. 7b. Thus, the flow fields predicted in the LBM simulation and measured in the experiment agree well for $\mathrm{Re} = 3 \times 10^5$, not only in one-point statistics and instantaneous time series, they also both uncover the mean flow structure.

5 Conclusion

The phenomenon of bi-stability in the flow around a sphere mounted on a CSR has been studied by means of experiments and LBM simulations. For $\mathrm{Re} = 10^5$, both methods show bi-stable side forces, involving similar time scales. For $\mathrm{Re} = 2 \times 10^5$, on the contrary, the experiment still reflects bi-stability, whereas the LBM simulation does not. This also leads to a lower drag coefficient in the LBM simulation, as bi-stability is known to be a drag contributor [5]. For $\mathrm{Re} = 3 \times 10^5$, neither the LBM simulation nor the experiment show any bi-stability. Regarding the average structure of the wake flow for $\mathrm{Re} = 3 \times 10^5$, an oil-film visualisation agrees well with the vortical structures found in the flow fields predicted by the LBM.

Further work needs to be contributed to the observed differences at $\mathrm{Re} = 2 \times 10^5$, as it is not clear, why the LBM is not able to resolve the bi-stability. The quantitative differences between the results predicted by the LBM and measured in the experiment for $\mathrm{Re} = 10^5$ might have multiple reasons: First, the inflow conditions are different. In the experiment, for example, the gust generator acts as an obstacle in the approaching flow. This was not considered in the LBM simulation, which was performed for an inflow with a constant velocity modulated by artificial turbulence. Second, small geometrical imperfections of the sphere used in the experiment might have affected the wake, as the latter is known to be sensitive to small changes. In the LBM simulation, on the other hand, the sphere is modelled as a smooth surface. Third, the LBM simulation requires turbulence modelling, as it is not possible to resolve all scales for the Reynolds number regime of interest. Nevertheless, it was shown that the LBM is able to predict the wake instability for $\mathrm{Re} = 10^5$, and match the turbulent wake for $\mathrm{Re} = 3 \times 10^5$.

Acknowledgements. Provided computing resources on DLR's CARA cluster and proof-reading by Annika Köhne are gratefully acknowledged.

References

1. Schroeck, D., Krantz, W., Widdecke, N., Wiedemann, J.: SAE Int. J. Passenger Cars Mech. Syst. **4**(1), 108 (2011). https://doi.org/10.4271/2011-01-0154
2. Ferrand, V.: J. Fluids Eng. **136**(1), 011101 (2014). https://doi.org/10.1115/1.4025466
3. Krajnović, S.: Int. J. Railway **1**(3), 99 (2008)
4. Grandemange, M., Gohlke, M., Cadot, O.: J. Fluid Mech. **722**, 51 (2013). https://doi.org/10.1017/jfm.2013.83
5. Pavia, G., Passmore, M., Sardu, C.: Evolution of the bi-stable wake of a square-back automotive shape. Exp. Fluids **59**(1), 1–20 (2017). https://doi.org/10.1007/s00348-017-2473-0
6. Gentile, V., van Oudheusden, B.W., Schrijer, F.F.J., Scarano, F.: J. Fluid Mech. **813**, R3 (2017). https://doi.org/10.1017/jfm.2017.4
7. Bury, Y., Jardin, T.: Phys. Lett. A **376**(45), 3219 (2012). https://doi.org/10.1016/j.physleta.2012.09.011
8. Constantinescu, G., Squires, K.: Phys. Fluids **16**(5), 1449 (2004). https://doi.org/10.1063/1.1688325
9. Müller, M., Ehrenfried, K., Bell, J., Wagner, C.: Analysis of model mount configurations with regard to force measurements with transient inflow. In: Dillmann, A., Heller, G., Krämer, E., Wagner, C., Tropea, C., Jakirlić, S. (eds.) DGLR 2018. NNFMMD, vol. 142, pp. 684–694. Springer, Cham (2020). https://doi.org/10.1007/978-3-030-25253-3_65
10. Chen, S., Doolen, G.D.: Annu. Rev. Fluid Mech. **30**(1), 329 (1998). https://doi.org/10.1146/annurev.fluid.30.1.329
11. Bhatnagar, P.L., Gross, E.P., Krook, M.: Phys. Rev. **94**(3), 511 (1954). https://doi.org/10.1103/PhysRev.94.511
12. Jeong, J., Hussain, F.: J. Fluid Mech. **285**, 69 (1995). https://doi.org/10.1017/S0022112095000462